

Additive Manufacturing of High-Gamma Prime Nickel-Based Superalloys through Selective Laser Melting (SLM)

Amrita Basak

Department of Mechanical Engineering
Pennsylvania State University, University Park, PA 16802, USA, Email: aub1526@psu.edu

Abstract

High- γ' nickel-based superalloys are abundantly used in the aerospace, marine, nuclear, and chemical industries where excellent corrosion and oxidation resistance, superior mechanical properties, and exceptional high-temperature performance are required. However, selective laser melting (SLM)-based additive manufacturing (AM) of high- γ' nickel-based superalloys pose significant challenges due to these alloys' complex chemistry. With multiple alloying elements and high aluminum + titanium fraction, these materials when consolidated through SLM form various secondary phases severely affecting the processability leading to the formation of cracks. The objective of this review is to summarize the progress made so far on SLM of high- γ' nickel-based superalloys with a special emphasis towards elucidating the relationships between processing, microstructures, and properties in this alloy system.

Keywords: *High- γ' Nickel-Based Superalloys, Additive Manufacturing, Selective Laser Melting (SLM), Processing, Microstructure, Mechanical Properties*

1. Introduction

High- γ' nickel-based superalloys are abundantly used in aircraft and power generation turbines, rocket engines, and other high-temperature environments because of their excellent corrosion and oxidation resistance, and superior mechanical properties [1]. Higher thermal gradients, thermal cycling and strains in gas turbine hot-section components cause severe fatigue loading, leading to fatigue cracking and spallation. The overall complexity associated with processing advanced hot-section high- γ' nickel-based superalloys through additive manufacturing (AM) originates from the fact that while these alloys can be cast into complex shapes through expensive and exotic investment casting techniques, once cast, these alloys are considered non-weldable or non-joinable. A key source of non-weldability is due to the presence of the secondary γ' precipitate phases in high proportion (i.e. more than 60 vol. %) in these alloys arising from combined additions of aluminum (Al) and titanium (Ti) [2, 3]. While these additions provide excellent benefits in improving overall high-temperature creep properties in new castings, they cause different types of cracking such as solidification, grain boundary liquation, strain-age, and hot tearing [1].

The presence of high- γ' fraction (which is an obvious peril of Ti + Al addition) increases the likelihood of cracking during post-weld heat treatment known as “strain-age cracking” [4]. The alloys also become susceptible to ductility-dip cracking associated with the formation of grain boundary carbides [5]. Based upon the compositions of %Al + 0.84 %Ti (in wt. %) versus 0.28 %Cr + 0.043 %Co (in wt. %), the relationship between the alloy chemistry and the weld susceptibility is illustrated in Figure 1 [6]. While the alloys belonging to the “non-weldable”

category are the most difficult one to fabricate, the “difficult-to-weld” alloys offer many issues as they are susceptible to heat affected zone (HAZ) cracking which is also known as hot cracking or solidification cracking. The alloys belonging to “fairly-weldable” category offers difficulties with post weld heat treatment (PWHT) operations resulting in crack formations [7]. While all the AM processes work on the fundamental principle of building an object through layer-by-layer fabrication, each differs with respect to the material delivery as well as the material consolidation mechanisms. The two primary classifications of the metal AM are directed energy deposition (DED) and powder bed fusion (PBF) [8, 9]. The material delivery for DED can be either via powder-blown or wire-fed mechanism and the energy source can be either a laser or an electron beam. Hence, in DED material is deposited where it is required. On the other hand, in PBF, the powder is spread in layers and selectively consolidated. Like wire fed DED, the energy source for PBF can also be either a laser or an electron beam.

Selective Laser Melting (SLM) is a PBF-based AM process that that uses high intensity laser as an energy source to melt and fuse selective regions of powder, layer by layer, according to computer aided design (CAD) data. SLM has been shown to be capable of producing fully dense near net-shape components without the need for post-processing through complete melting

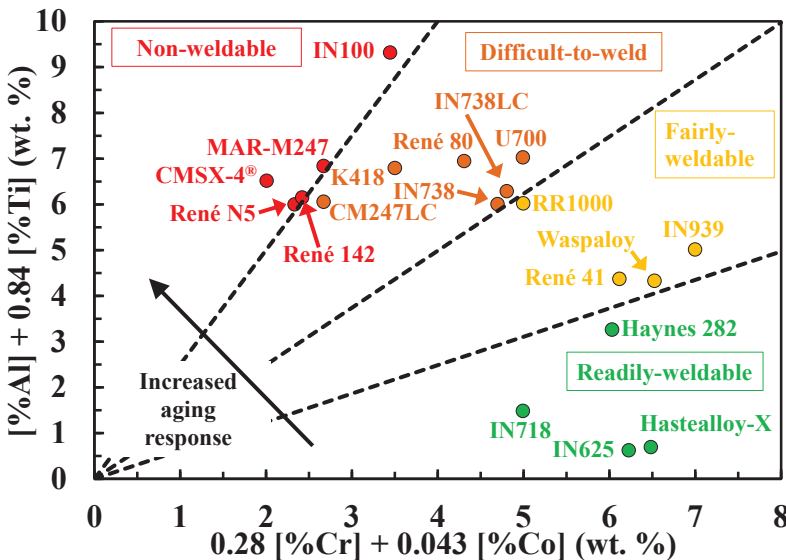


Figure 1. Weldability assessment for nickel-based superalloys (adopted from [6]).

nickel-based superalloys [8-12], a focused review on the SLM-based processing of an important class of material system such high- γ' nickel-based superalloys, is still missing. The objective of this review is to summarize the progress made to date on these alloy systems with a special emphasis towards elucidating the relationships between processing, microstructures, and properties facilitating direct manufacturing of high- γ' nickel-based superalloys such as CM247LC [13-18], CMSX-4®[19-23], MAR-M247 [24-26], IN100 [27, 28], IN738LC [29-36], K418 [37], René 142 [38-40], René 80 [41], and René N5 [6, 42, 43] for high-temperature applications. The review also identifies the potential areas of future research that is required to advance the field of SLM of high-performance material systems.

the powder material. However, like other AM processes, SLM parts are subjected to complex thermal cycles including repeated heating and cooling due to melting and solidification, respectively. Such alternating thermal cycle creates residual stress in the part as well as heterogeneity and anisotropy in the part's microstructures and properties [10]. SLM of high- γ' nickel-based superalloys pose additional challenges due to these alloys' complex chemistry. Although, several review articles are available on AM of metallic materials and

2. Selective Laser Melting (SLM)

SLM starts with a CAD model of the part that is sliced at discrete intervals in the build direction. The resulting cross-sections are stored sequentially in a “build file”. Scanning algorithms are devised to plan the path of the laser beam. The powder bed is sintered conforming to the geometry requirement for the layer [12]. Next, the powder bed is lowered by a distance

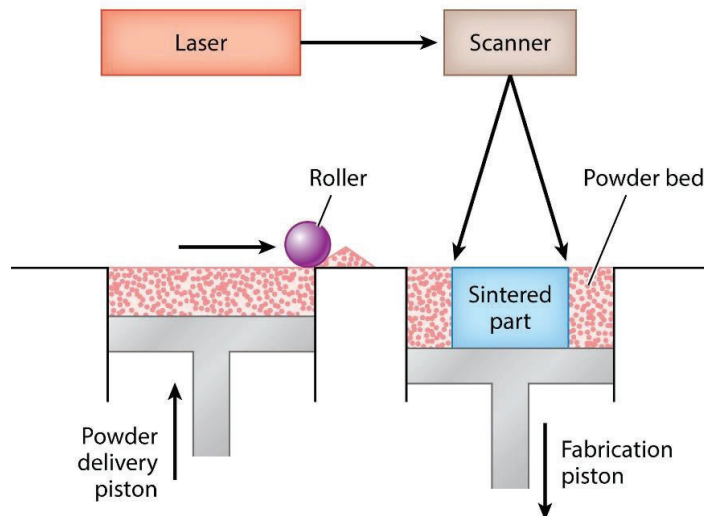


Figure 2. Overview of the SLM process (adopted from [8]).

equal to the layer thickness and a fresh layer of powder is deposited by a roller or cassette mechanism. The next cross-section is then laser-fused deeply enough to continuously bind it to the underlying layer, and thus, by fusing layer upon layer, the entire part is fabricated. The schematic of the process is shown in Figure 2. The components created through direct SLM processes are fully dense or nearly fully dense and can be post-processed using hot isostatic pressing (HIP) to achieve full density through the closure of any residual porosity.

High power CO₂, Nd:YAG, and Yttrium lasers are typically used as the energy source in SLM. The average layer thickness for SLM ranges from 20 μm – 100 μm for multi-pass fabrication [44]. For single-pass repairs, the powder layer thickness can go up to 2000 μm [19]. The laser beam can go up to scan speed of 15 m/s. The typical spot size ranges from 40 μm – 180 μm in diameter [45]. SLM can be conducted at extremely pure inert environment with less than 10 PPM O₂ level in order to minimize oxidation. The powder bed can be kept at atmospheric or elevated temperatures depending on the application requirement. The SLM system has the flexibility to be operated with open loop or closed loop control schemes facilitating a tighter control of the melt pool temperature [12] [46]. In SLM, preheat temperature in the range of 90 – 1200 °C has been reported in literature for processing high- γ' nickel-based superalloys [26]. Scanning laser epitaxy (SLE) deserves a special mention in this regard as this process does not preheat the powder bed at all [19, 20].

The parts fabricated through SLM have higher dimensional accuracy and surface smoothness than DED. Since, the part is immersed in the powder bed; this process also has advantages as the bed acts as a support structure. However, since this process requires a controlled manufacturing atmosphere, the size of build chamber, and therefore, the part is limited. Like DED or EBM processes, due to rapid alternating thermal cycles, the parts may develop residual stresses requiring further post processing. Laser powder bed fusion processes have high cooling rates, varying between $\sim 10^4$ and 10^6 K s^{-1} . On the other hand, processes like EBM use a hot bed ($>870 \text{ K}$) reducing the cooling rate and hence do not produce a fine microstructure like the laser powder bed fusion process [47]. Since, the SLM involves partial or

complete melting of previous layer(s), the grain structure in the current layer is controlled by that of the previous layer.

3. Nickel-Based Superalloys

Nickel-based superalloys generally contain several different alloying elements to attain the desired property level for hot rupture strength, fatigue resistance, and creep strength. Typically, high-gradient casting (investment casting with high and well controlled thermal gradient) is used to develop customized and fine structured superalloys, although some wrought superalloys are also in use. Properties of the superalloys are controlled by the presence of different phases in the microstructures such as the close packed phases (γ' , γ'' , and η etc.) and the carbides (MC , M_6C , $M_{23}C_6$ where M denotes the metal) [1]. Nickel-based superalloys primarily consist of intermetallic precipitates in a solid solution of face-centered cubic (FCC)-Ni matrix or γ matrix. The intermetallic precipitates are known as γ' , and a high-volume fraction of γ' (up to 70%) is typically added to improve the strength of the γ -matrix. The γ' phase is chemically represented as $Ni_3(Al, Ti)$, with Al and Ti replacing the corner Ni atoms in an FCC structure and forming a coherent phase with FCC- L_{12} phase. The secondary phase precipitates retard dislocation motions by forming anti-phase boundaries and locking the dislocations at high temperatures [48, 49].

Table 1. Nominal composition of high- γ' nickel-based superalloys that are processed using SLM to date (wt. %)

	CM247LC	CMSX-4®	IN100	IN738LC	K418	MAR-M247	René 142	René 80	René N5
Cr	8.1	7.6	10	16	12.5	8	6.8	14	7.1
Co	9.2	9.3	15	8.5	-	10	12	10	8
Mo	0.5	0.4	3	1.75	4.3	-	1.5	4	2
Re	-	1	-	-	-	-	2.8	-	3
W	9.5	2	-	2.6	-	10	4.9	4	5
Al	5.6	12.6	4.7	3.4	6.2	6	6.15	3	6
Ti	0.7	1.3	5.5	3.4	0.7	1	-	5	-
Ta	3.2	2.2	-	1.7	-	3	6.35	-	7
Hf	1.4	0.03	-	-	-	1	1.5	-	-
Nb	-	-	-	0.9	2.1	-	-	-	-
B	0.015	-	0.014	0.1	0.014	0.015	0.015	-	-
C	0.07	-	0.18	0.11	0.12	0.15	0.12	-	-
Zr	0.015	-	0.06	0.05	-	0.05	0.02	-	-
Fe	-	-	-	-	1	-	-	-	-
Ni	Bal	Bal	Bal	Bal	Bal	Bal	Bal	Bal	Bal

Cr = chromium, Co = cobalt, Mo = molybdenum, Re = rhenium, W = tungsten, Al = aluminum, Ti = titanium, Ta = tantalum, Hf = hafnium, N = nitrogen, B = boron, C = carbon, Zr = zirconium, Fe = iron, Ni = nickel.

Careful element addition is necessary in superalloys, since some elements facilitate the formation of brittle plate-like μ , σ , or Laves phases [1]. The μ phase is typically of rhombohedral crystal structure and is found in alloys with excess percentage of Mo or W. The σ phase is a tetragonal phase that forms after prolonged exposure to a temperature between 540 °C and 980

°C. The hexagonal Laves phase is formed due to high-temperature exposure. These phases are topologically close-packed (TCP) phases and cause reduction in rupture strength and ductility [50]. Table 1 documents the nominal composition of high- γ' nickel-based superalloys that are processed using SLM to date.

Different forms of cracking are present in SLM of nickel-based superalloy components. They can be primarily distinguished as solidification cracking, grain boundary liquation cracking/hot tearing, strain-age cracking (cold cracking) and ductility dip cracking [51]. Solidification cracking occurs when the mushy, two-phase liquid-solid region experiences tensile stresses and the high fraction of solid present (typically solid fraction > 0.9) restricts the flow of liquid metal to backfill the interdendritic regions [52]. The interdendritic regions are torn apart by tensile thermal stresses generated behind the melt pool as it progresses. Formation of solidification cracking is promoted by a wide solidification range for the alloy and low scan speeds. Local or partial dissolution of grain boundary phases leads to the formation of low melting point eutectics and melting of grain boundary regions, thus, leading to grain boundary liquation cracking or hot tearing when the liquid film in HAZ fails under tensile stress. Typically, the intermetallic carbide compounds (MC and M_6C) and different secondary phases (Laves- and σ -phases) contribute to partial dissolution, and hence, reduction of the melting point. Different impurities such as sulfur, boron, and phosphorus act to suppress the eutectic melting temperature and consequently increase the HAZ fissuring susceptibility [1]. A second mechanism known as constitutional liquation particular to precipitation-hardened materials occurs when a constituent particle such as TiC reacts with the surrounding matrix causing localized melting. Creation of smaller grains exposes more boundary area and lowers the strain value, resulting in reduction of hot tearing. It is also verified that processing conditions such as heating rate affect the formation of this kind of cracks. Higher power results in more area being liquated increasing the tendency of HAZ cracking [1].

4. Effects of Powder Properties

Due to their much higher surface area per unit volume compared to cast or wrought component, powder metallurgy-based AM processes such as SLM typically have a higher degree of contamination. These contaminants adversely affect the mechanical properties of the final parts [53]. Table 2 lists the powder material properties that can significantly affect the properties of the SLM fabricate components [54, 55]. Powders used in SLM are produced via plasma, gas, or water atomization processes. In gas atomization, the molten material is atomized by inert gas jets and the resulting metal droplets are cooled in the atomizing tower. Metal powders obtained by gas-atomization typically show spherical particles. The powder quality depends on the properties of the atomizing gas such as type and pressure. The molten metal is typically produced by vacuum induction melting or electron induction melting. The gas-atomization method also works for both reactive and non-reactive material systems. In plasma atomization, metal wires that are fed into the tip of multiple plasmas, melt and are atomized in a single step. In water atomizing, a falling stream of molten metal is impinged with jets of water which immediately solidify the metal into granules (>1 mm) or powder (<1 mm). The atomization processes critically affect the powder properties such as particle size, morphology, and chemical composition impacting the final part properties. Table 3 documents the powder properties of several high- γ' nickel-based superalloys that are processed using SLM to date.

Table 3. SLM process parameters and material variables influencing the processing and densification mechanism of fabricated parts [54, 55].

SLM processing parameters	Material properties
Laser power	Viscosity
Scan rates/scan speed	Surface tension
Atmospheric control	Particle size and distribution
Gas flow	Particle shape
Heaters (bed temperature)	Absorptivity/reflectivity
Laser type	Thermal conductivity
Scan radius	Specific heat
Scan vector length	Emissivity
Scan spacing	Melting temperature
Thickness of layers	Component ratio
Machine (specific type)	Chemical composition

Table 4 Details of nickel-based superalloy powders used in SLM.

Material	Supplier	Particle Size (μm)	AM System	Reference
CM247LC	LPW Tech. Ltd.	15-70 (Log-normal)	SLM	[13, 14]
	LPW Tech. Ltd.	15-53	Concept Laser M2	[15, 18]
	-	-	EOS M280	[16]
	LPW Tech. Ltd.	15 – 100 ($D_{10} = 20$, $D_{50} = 36.4$, and $D_{90} = 57.1$)	Realizer SLM 50	[17]
CMSX-4 [®]	Praxair Surface Technologies	20-150	SLE	[19-23]
IN100	Pratt & Whitney – HMI Metal Powders	20-150	SLE	[27, 28]
IN738LC	Nanoval	6-41	Concept Laser M1	[29, 36]
	-	27.9\10.2 (Log-normal)	SLM	[30]
	-	$D_{10} = 6$, $D_{50} = 22$ and $D_{90} = 41$	Concept Laser M2	[31]
	H.C. Starck	10-50	EOS M280	[32]
	Carpenter	20-70	EOS M280	[33]
	-	A: $D_{10} = 8$, $D_{50} = 17$, $D_{90} = 33$ B: $D_{10} = 10$, $D_{50} = 19$, $D_{90} = 34$ C: $D_{10} = 8$, $D_{50} = 20$, $D_{90} = 42$ D: $D_{10} = 11$, $D_{50} = 24$, $D_{90} = 50$	Concept Laser M2	[34]

		E: D ₁₀ = 8, D ₅₀ = 18, D ₉₀ = 35 F: D ₁₀ = 7, D ₅₀ = 16, D ₉₀ = 32 G: D ₁₀ = 23, D ₅₀ = 36, D ₉₀ = 49 H: D ₁₀ = 10, D ₅₀ = 16, D ₉₀ = 27		
	Erasteel	D ₁₀ = 20, D ₅₀ = 33, D ₉₀ = 55	SLM 280 HL	[35]
K418	Beijing AMC Powder Metallurgy Technology Co, Ltd.	10–80, mean = 28.59	Self-developed SLM machine (SLM-100, Xi'an Jiaotong University, China)	[37]
MAR-M247	Praxair Surface Technologies	20-50	SLE	[24, 25]
	IKTS	D ₅₀ = 47	HT-SLM	[26]
René 142	Carpenter Technology Corporation	30 - 110	SLE	[38-40]
René 80	Pratt & Whitney - HMI Metal Powders	20-150	SLE	[41]
René N5	Praxair Surface Technologies	20-120	SLE	[6, 42, 43]

Table 4. Composition of the powder batches. The first two rows show the min./max. values for the cast version of this alloy according to the technical datasheet Alloy IN738 Technical Data (1981)(adopted from [34]).

	Main alloying elements [wt%]												Residual elements [wt%]		
	Ni	Cr ^a	Co ^a	Mo ^a	W ^a	Ta ^a	Al ^a	Ti ^a	Nb	C	B	Zr	Si	Fe	Cu
Min.	Balance	15.7	8.0	1.5	2.4	1.5	3.2	3.2	0.6	0.09	0.007	0.02	–	–	–
Max.		16.3	9.0	2.0	2.8	2.0	3.7	3.7	1.1	0.13	0.012	0.08	0.3	0.05	–
A		15.8	8.6	1.7	2.6	1.7	3.5	3.3	0.80	0.096	0.011	0.060	0.085	0.06	0.011
B		16.1	8.5	1.7	2.6	1.8	3.5	3.4	0.85	0.097	0.010	0.065	0.064	0.08	0.012
C		16.1	8.8	1.8	2.4	2.9	3.5	3.5	0.75	0.130	0.012	0.652	0.105	0.11	0.611
D		15.9	8.4	1.8	2.6	2.0	3.4	3.5	0.80	0.110	0.013	0.041	0.030	0.06	0.164
E		16.2	8.6	1.8	2.7	1.7	3.5	3.3	0.80	0.140	0.015	0.023	0.034	0.82	0.099
F		16.1	8.4	1.7	2.7	1.7	3.5	3.7	0.80	0.140	0.012	0.056	0.212	0.13	0.004
G		16.0	8.6	1.6	2.8	1.8	3.5	3.4	0.90	0.120	0.009	0.011	0.026	0.15	0.001
H		15.9	8.3	1.8	2.6	1.9	3.5	3.3	0.80	0.096	0.014	0.032	0.018	0.09	0.004

^a values according to the suppliers material certificate.

Table 5. Trace element and gas content of the powder batches (adopted from [34]).

	Trace elements [ppm]													Gas content [ppm]		
	S	Mn	Hf	P	Ag	Bi	Se	Te	Tl	Pb	Ga	Mg	Sn	O ₂	N ₂	H
A	6	17	50	42	4.5	2.0	32	1.0	4.1	2.4	15.9	26	4.0	300	36	8
B	7	22	53	<3	3.4	1.3	8	2.8	2.6	3.8	15.0	30	3.8	160	8	10
C	46	121	3	<3	7.2	1.1	15	0.7	0.1	7.4	11.9	23	6.2	320	12	8
D	4	18	89	<9	1.4	0.7	25	0.2	2.3	1.9	6.6	40	1.8	290	17	8
E	5	101	4	<9	1.0	0.6	24	0.6	2.6	2.1	12.0	23	85.7	400	19	8
F	6	18	0	<9	1.3	0.5	31	0.8	2.5	22.5	17.1	30	10.1	1000	78	30
G	7	67	331	32	0.4	0.1	30	0.3	1.8	0.9	10.8	13	1.9	190	15	5
H	<4	147	92	<9	10.7	0.2	27	<0.1	2.6	0.2	5.4	34	4.5	360	11	9

Figure 3. SEM images of the powder batches showing particle morphology (adopted from [34]).

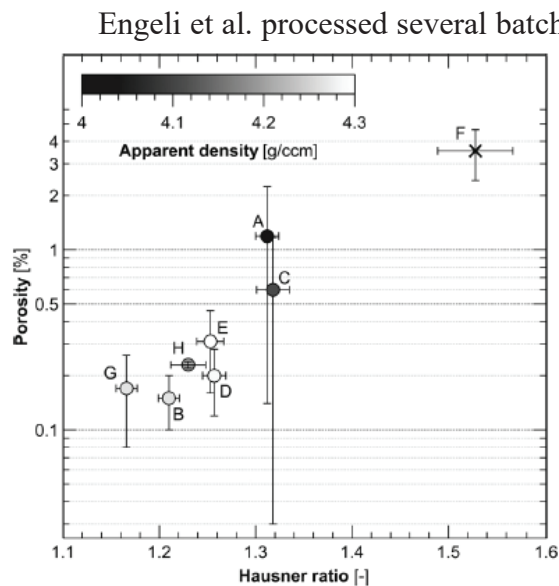
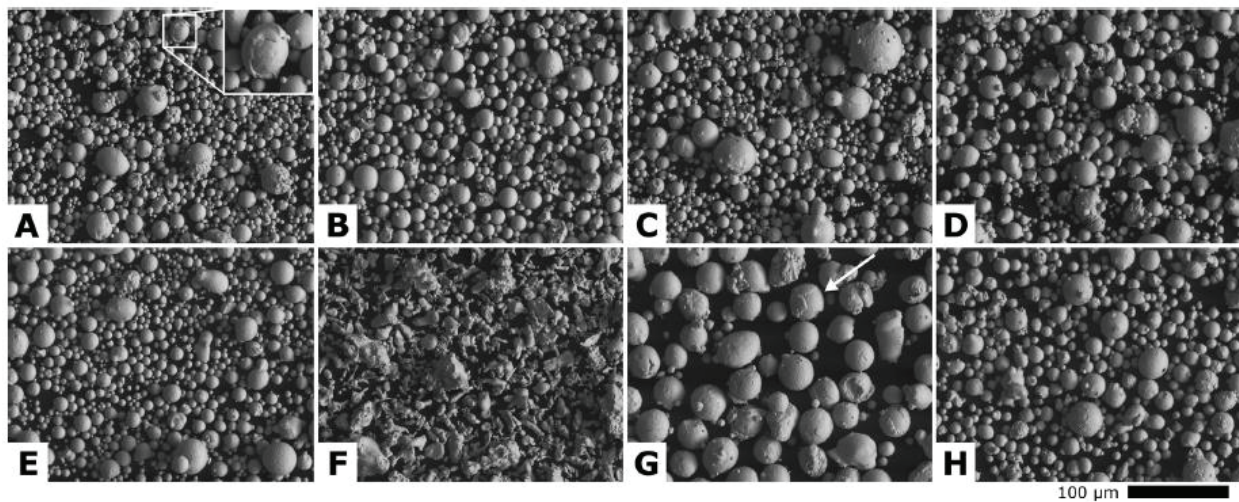


Figure 4. Porosity in the SLM processed sample versus the Hausner ratio of the corresponding powder batch. The apparent density of the powders is color coded in grayscale, with exception of batch F which is out of bound of the applied color scale (adopted from [34]).

Engeli et al. processed several batches of commercially available IN738LC powder made by gas and water atomization under identical processing conditions [34]. Tables 4 and 5 list the powder composition. All powders were gas atomized (GA) except for batch F which was water atomized (WA). Powder batches D, E, and H were atomized from vacuum molten feedstock material (VMF), whereas batch C was directly alloyed from the elemental raw materials. No information was available for powder batches A, B, F, and G. To assess the flowability, the Hausner ratio, defined as the ratio between the tapped and apparent density, was used. A low Hausner ratio represents a good flowability. Figure 3 shows the SEM images of the powder particles. A striking difference may be observed for WA batch F that does not show any spherical powder particles at all.

Engeli et al. reported specimens with a density > 98.2% for all GA powder batches [34]. The process parameters optimized for powder batch H, were suitable to process all GA powder batches despite the differences in their particle size distribution and composition. Batches A and C showed higher porosity due to their high Hausner ratio. A low flowability can result in a local starvation of powder after recoating. The

correlation between the porosity and the Hausner ratio of the corresponding powder batch is shown in Figure 4. The poor flow behavior of the powder batches F, A, and C resulted in the

lowest measured apparent density of the specimens. WA powder batch showed a considerably higher due to poor flowability resulting in poor recoating behavior. Another potential reason is due to the higher oxygen content of WA powder that results in increased oxidation and decreased wettability behavior of the melt pool.

Engeli et al. reported a large variation of crack densities ranging from 0.3 mm/mm² up to 4.5 mm/mm² different batches of IN738LC [34]. The best linear correlation with the crack density was found with Si, followed by the Ga and Pb content as shown in Figure 5. Risse et al. showed that the crack density in SLM processed IN738LC was influenced by the melt pool size, however, no correlation between the melt pool size and crack density was reported [56]. With respect to the composition, in conventional welding, certain elements have been shown to increase susceptibility to cracking [57]. Rappaz et al. introduced the concept of “attractive” and “repulsive” grain boundaries [58]. The authors proposed that two approaching grains would coalesce when the energy required to create a grain boundary is lower than the energy of two solid–liquid interfaces. On the contrary, a repulsive grain boundary would have a thin liquid film between the grains until a certain undercooling is reached, which increases the susceptibility to hot cracking. Potential changes of the grain boundary or solid-liquid energies by Si would promote cracking during solidification. Zhu et al. reported that the segregation of Si increased with increasing solidification velocity. The effect of Si would therefore be amplified by the rapid solidification during SLM [59].

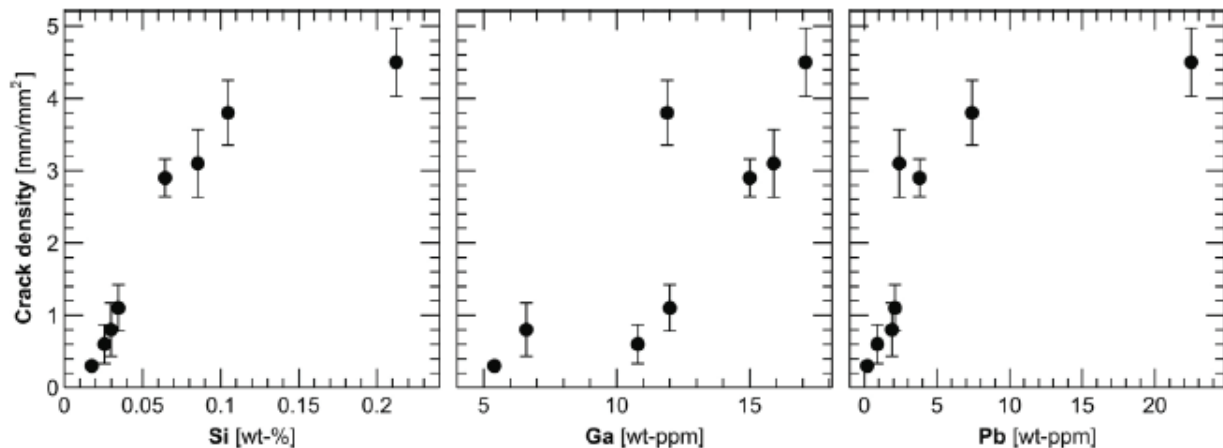


Figure 5. Crack density measured for the different powder batches plotted versus their Si, Ga, and Pb content (adopted from [34]).

5. Effects of Processing Conditions

Characteristics of SLM fabricated deposits are a strong function of the processing conditions as well as process history. The cooling rates are extremely high ($\sim 10^6$ K/s) in SLM. Basak et al. reported the single pass fabrication of CMSX-4[®] specimens using SLM [19]. The authors used an additional parameter, number of repeat scans (N) to establish a steady melt pool in the beginning of the scan. N was defined as the number of raster movements that the laser performed at the leading edge of the specimen without moving in the forward direction during the start of the scan process. Reduced N resulted in discontinuous substrate-powder metallurgical bond; however, increased N caused excessive melt back near the starting edge. Similarly, if the

scan speed was too high, there would be a thermal lag, resulting in deformation or warping of the sample as shown in Figure 6.

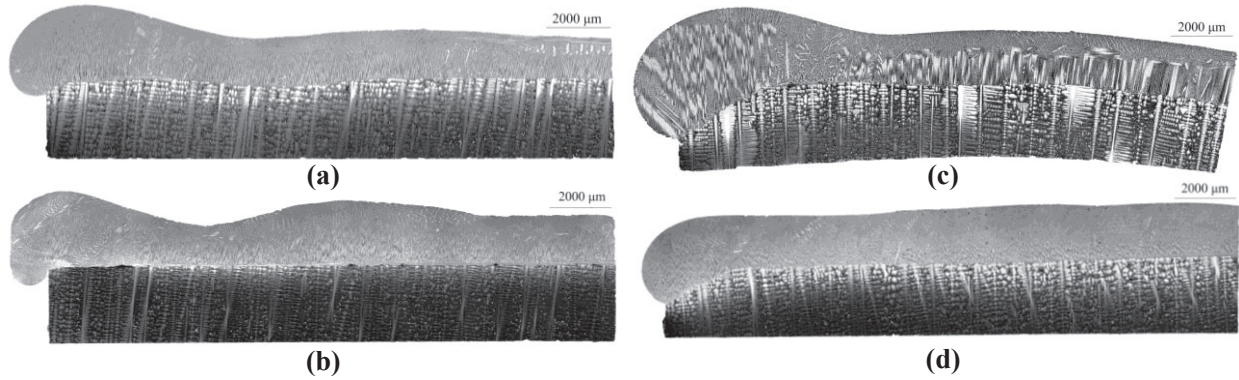


Figure 6. Representative transverse optical micrograph of CMSX-4® deposit showing (a) crack-free and dense deposit, (b) lack of fusion due to reduced number of repeat scans, (c) deformation/warping due to higher scan speed, and (d) lower single crystal height due to lower scan spacing (adopted from [19]).

A. Densification

Perevoshchikova et al. used Doehlert matrices to investigate the influence of the three

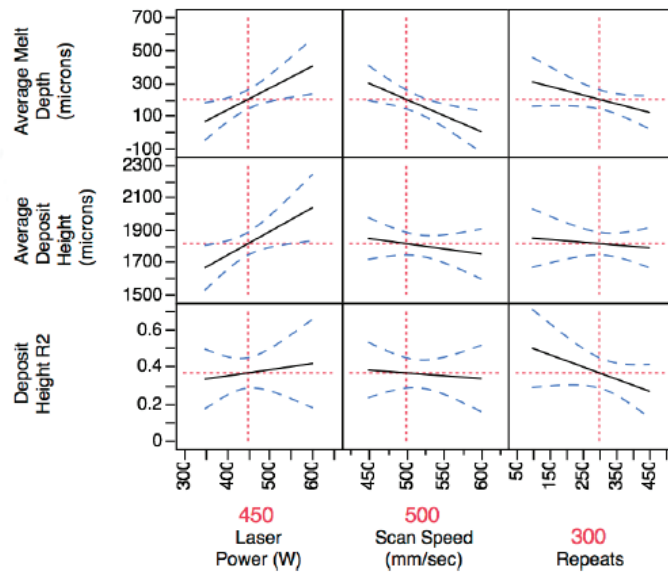


Figure 7. Overview of the effects of each process parameter on the various quality metrics for René 80 deposits [41].

processing parameters (scan speed, power, and hatching distance) to arrive at a set of optimal parameters to meet the component densification objective [33]. The experimental field was defined as power (P) ranging from 270-370 W, scan speed (V) ranging from 850-2250 mm/s, and hatching spacing (h) 0.09-0.13 mm. The result of Doehlert design with three parameters was a second-order equation with one constant term, three linear terms, three interaction terms and three-square terms: $Y = a_0 + a_1X_1 + a_2X_2 + a_3X_3 + a_{11}X_1^2 + a_{22}X_2^2 + a_{33}X_3^2 + a_{12}X_1X_2 + a_{13}X_1X_3 + a_{23}X_2X_3$. Here X_1 , X_2 , and X_3 were coded factors, and Y was estimated response. Coefficients $a_0 \dots a_{23}$ were evaluated from Y and X_1 , X_2 , and X_3 using: $a = (X_t X)^{-1} X_t Y$ where $X_t = (X)^T$. In this study, the relative density of sample, ρ

(defined as the ratio of specimen density over theoretical density) was the evaluation indicator of response Y , considering the influence of three variables, power (X_1), scan speed (X_2) and hatching distance (X_3). The relative density as a function of energy density of SLM-processed

test specimens using both Archimedes method and microstructure. From these results, the authors concluded that maximizing the energy density was not a suitable approach for maximizing density. The relative density significantly reduced with an increase in V and h , and decreased with an increase in P .

B. Deposit Characteristics

Acharya et al. implemented Phase 1 ascent design of experiments (DoE) methodology based on a fractional factorial design to evaluate the effects of P , V , and N on the deposit characteristics such as deposit uniformity, melt depth, and deposit height for René 80 [41]. The explored range of parameters included 100 – 400 repeat scans, 450 – 650 mm/s scan speed, 12.7 mm hatch spacing, and 350 – 600 W laser power. The deposit uniformity was calculated by taking the deposit height of the specimen, developing a linear fit for the height and then calculating the average R^2 residual between the height and the linear fit. By definition, higher R^2 value implied more uniform deposit. P and V were both used to control the amount of energy being applied to the specimen during the fabrication process. N affected the formation of a melt pool at the start of the scan. Hence, an optimized value of N was required in order to establish a melt pool that propagated steadily fusing powder to the underlying layer. The authors reported that P impacted the deposit height and melt depth and increased each of these values as it increased (Figure 7). V impacted the melt depth and caused it to decrease as V increased. N impacted the deposit uniformity and melt depth, increasing both as N increased.

C. Microstructure

Microstructure of SLM deposited nickel-based superalloys typically show columnar, equiaxed or mixed microstructure depending on the thermal conditions and the cooling rates.

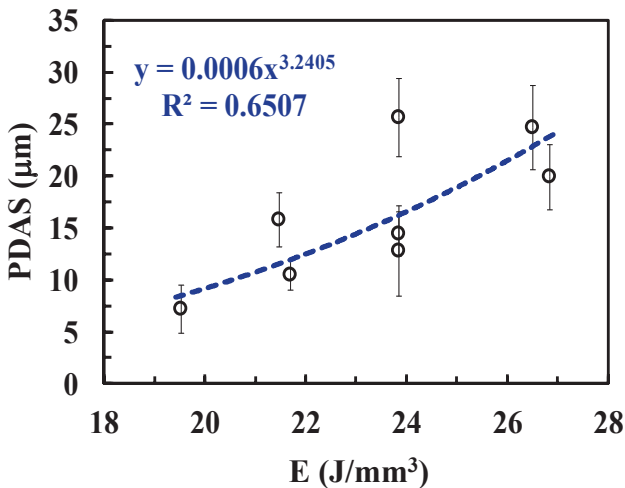


Figure 8. Effect of E on the PDAS [25].

While an equiaxed microstructure can be characterized by the grain size and distribution; a columnar microstructure requires several additional parameters such as the primary dendrite arm spacing (PDAS), the columnar-to-equiaxed transition (CET), the oriented-to-misoriented transition (OMT), and the presence of stray grains (SG) for accurate representation. An increase in PDAS adversely affects the high-cycle fatigue life [19]. During solidification, the solidified region acts as a heat sink, and the temperature gradient ahead of the solidification front decreases, resulting columnar-to-equiaxed transition or CET. A second solidification phenomenon, known

as the oriented-to-misoriented transition (OMT), occurs when there is a change in the direction of the temperature gradient in the solidifying metal. Existing literature reveals that the local inhomogeneity in the temperature gradient and the solidification velocity or the presence of broken dendritic arms and subsequent convection of those broken pieces acts as sources of new

nucleation sites that result in the formation of stray grains (SG) resulting in higher grain boundary wetting and making the material prone to cracking.

Basak et al. reported single pass depositions of CMSX-4[®] and the authors showed SGs decreased for higher values of energy density (E) [19]. Lower V and higher P caused smoother flow of powder and lowered the Marangoni velocity at the top surface of the melt pool, thus decreasing the convection of broken dendrites. This reduced stray grain formation. However, the columnar ratio decreased significantly for higher values of E. The higher laser powers and lower scan speeds expanded the melt pool, thus reducing the temperature gradient in the vertical direction. This caused nucleation of new grains due to constitutional undercooling resulting in

lower columnar ratios at higher values of E. Basak et al. also reported the effects of processing conditions on PDAS for MAR-M247 as shown in Figure 8 [25]. However, no current literature is available on the effects of processing conditions on precipitate size, composition or elemental segregation in the SLM fabricated nickel-based superalloys.

D. Metallurgical Defects

Several defects such as cracks, porosity, and oxide inclusions are found in the SLM fabricated nickel-based superalloys. Poor weldability of high- γ' nickel-based superalloys results in the formation of cracks in the SLM manufactured specimens. A traditional method of reducing build-up of residual stresses is to divide the build area of each layer into smaller square sections referred to as 'islands', consisting of a border and inner raster scan region. Variation in cracking density using 'island' scanning in CM247LC deposits was reported by Carter et al. [15, 18]. Catchpole-Smith et al. developed novel fractal scanning strategies based on mathematical fill curves, namely the Hilbert and Peano-Gosper curves (shown in Figure 9) for reducing residual stresses in SLM processed CM247LC specimens [17]. The highest XY plane bulk density of $98.0 \pm 0.1\%$ was achieved using the Peano-Gosper scan at 75 W laser power and 600 mm/s scan speed. This is significantly higher than the XY plane bulk density of the 'island' scan sample at $96.0 \pm 0.6\%$. This was attributed to the large amount of spherical porosity seen in the 'island' sample. On the contrary, porosity was rarely seen in any of the fractal scan samples.

Cloots et al. investigated the effects of Gaussian and a doughnut beam profile on the microstructure and crack formation of IN738LC [31]. Within the Gaussian series, V of 900 mm/s represented the inflection point between high and low porosity. In general, porosity within the Doughnut series

was higher due to bonding defects. Porosity caused by gas pores and spherical pores was

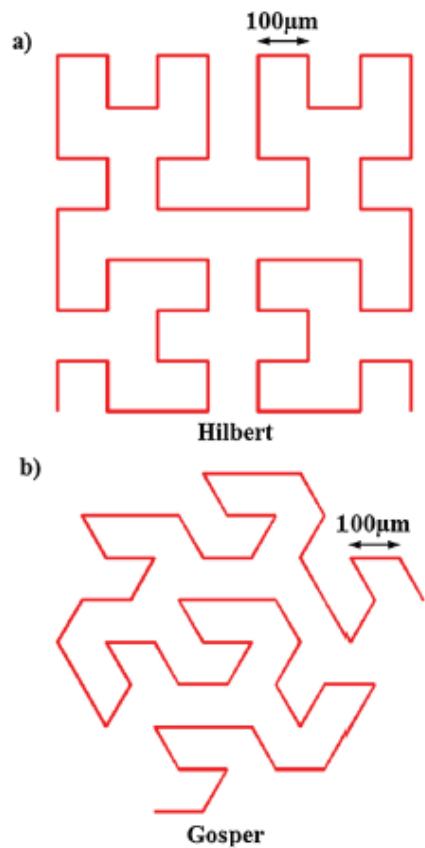


Figure 9. Illustration of the novel scan strategies generated using the (a) 3rd order Hilbert and (b) 2nd order Peano-Gosper mathematical area filling curves. The 100 μm characteristic scan vector length is shown (adopted from [17]).

relatively constant at 0.2% over the entire range of V. The crack density [mm/mm^2] defined as the ratio of the cumulated length of all cracks detected on a certain surface of each investigated sample was about $0.27 \text{ mm}/\text{mm}^2$ for Gaussian series. In contrast, the crack density within the Doughnut series at the same scan speed was only $0.11 \text{ mm}/\text{mm}^2$, thus, establishing benefits of the Doughnut series.

Qiu et al. showed the dependence of defects (pores and cracks) on laser processing parameters such as P and V [32]. With increased V, the pore size increased, and their shape became elongated due to lack of fusion. The crack density, in contrast, remained relatively constant with P within 200 – 360 W range. This was in sharp contrast with results on CM247LC that showed significantly high density of cracks [17, 18]. A significant number of cracks were found to extend along the grain boundaries (GBs). However, a few cracks initiated from the pores as well. Majority of cracks were found to be associated with the presence of particles or micro-segregation along GBs. Some particles were rich in Al and O implying the formation of Al_2O_3 . Other particles were rich in W, Si, and O, indicating that they could be a mixture of W- and Si-oxides such as WO_2 and SiO_2 . With regards to segregation, in the vicinity of the cracks; W, Si, and O were found to be segregated.

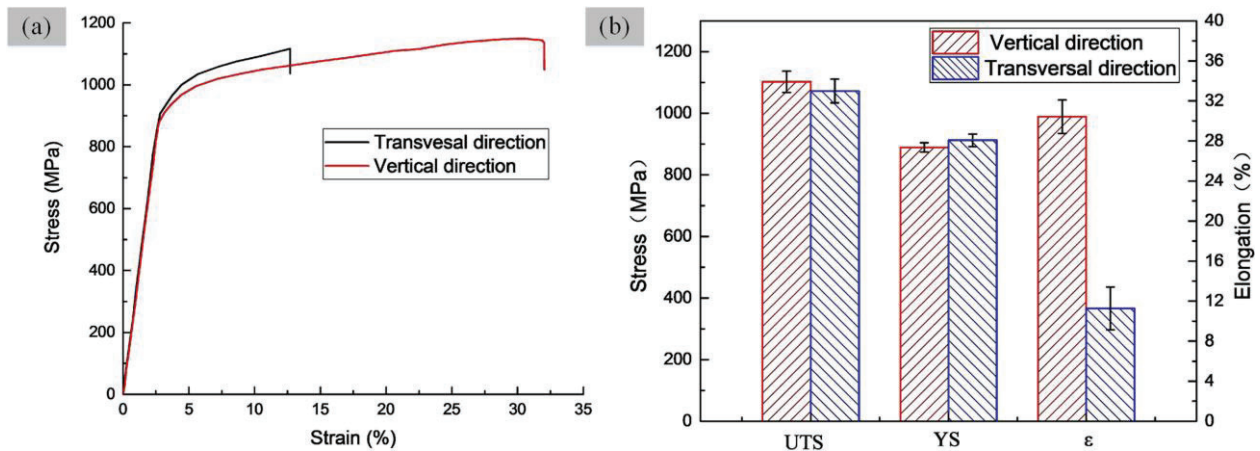


Figure 10. Mechanical properties of as-fabricated SLM specimens at room temperature, (a) Tensile test curves and (b) Corresponding mechanical data. (adopted from [37]).

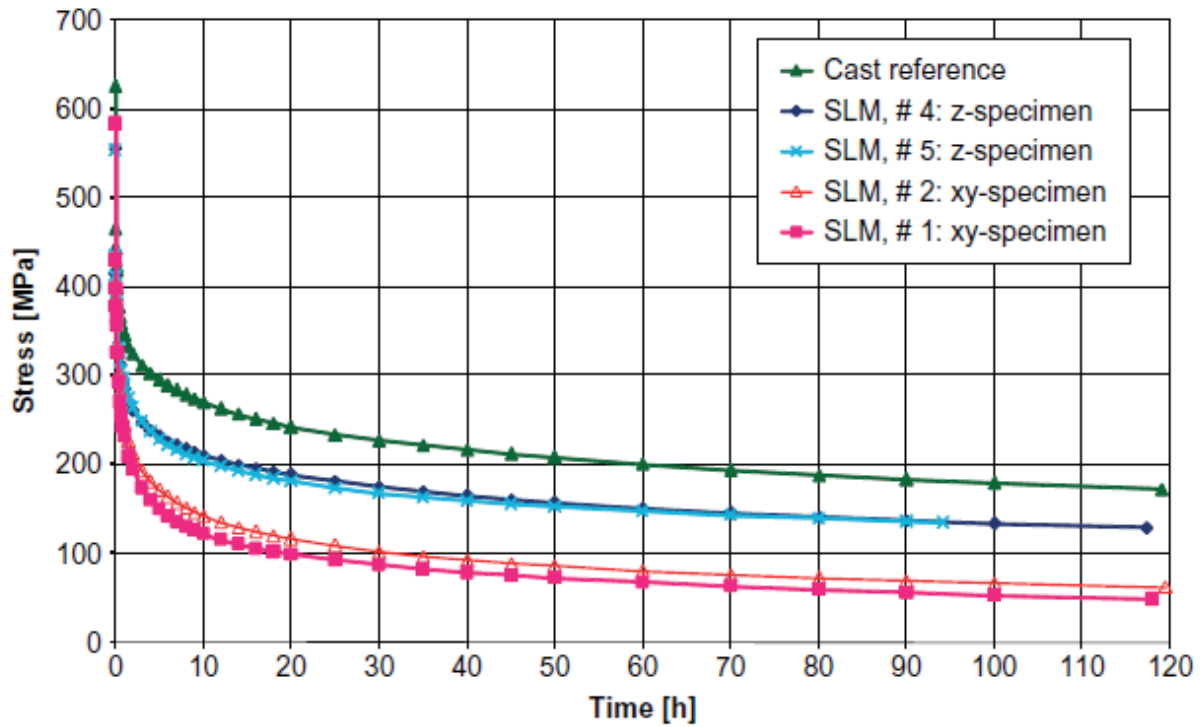
6. Mechanical Properties

A. Tensile Strength

Chen et al. investigated the tensile properties of the SLM-processed K418 specimens in the build and scan direction as shown in Figure 10 [37]. The tensile strength and ductility in both directions were larger than the casting probably due to the formation of the ultrafine columnar grains due to the high thermal gradient and the rapid cooling rate during SLM. The longitudinal specimens ($\epsilon = 30.42 \pm 1.68\%$) showed significantly higher elongation than the transverse ones ($\epsilon = 1.27 \pm 2.14\%$). The tensile loads were parallel to the columnar grain-boundary in vertical specimens as the plastic deformation was easier when the columnar grains were elongated. Rickenbacher et al. reported that the yield and ultimate tensile strength of IN738LC specimens

extracted from the scan direction were both 23% higher whereas the average elongation was identical with the mean values of cast specimens [29]. Specimens extracted along the build direction also showed superior yield and ultimate tensile strength with 3 and 23% higher values, respectively. However, they showed a 21% lower Young's modulus and a 49% higher elongation at break, indicating a more ductile material behavior in this direction. The difference in the properties was primarily attributed to the grain orientation and higher amount of transverse grain boundaries.

B. Relaxation Behavior



Note: A cast specimen was tested as reference

Figure 11. Relaxation behavior of SLM specimens, two built up along the z-axis and two within xy-plane (adopted from [29]).

Rickenbacher et al. reported the results from the relaxation tests at 850 °C as shown in Figure 11 [29]. As the specimens have different Young's moduli, the initial strain of 1% resulted in different stress levels. The relaxation behavior of the cast IN738LC specimens was superior compared to those manufactured by SLM. This behavior was either due to differences in grain size/grain orientation and/or due to differences in the γ' size and morphology. Another important difference between SLM and cast IN738LC specimens was the presence of the carbide precipitates. The specimens extracted from the scan direction showed inferior relaxation behavior and superior strength properties, while for the specimens extracted from the build direction showed the opposite behavior. Such behavior was probably due to fact that straining was primarily parallel to the columnar grains for the scan direction specimens while for the built direction specimens; strain/stress was applied transverse to the grain boundaries.

C. Creep

Results from 1,000 h and 3,000 h creep tests performed by Rickenbacher et al. confirmed the behavior of the relaxation tests [29]. Specimens extracted along the build direction showed superior creep properties compared to the specimens extracted from the scan direction, but slightly inferior compared to cast IN738LC as shown in Figure 12. SLM specimens showed lower creep rupture strengths. However, specimens extracted from the build direction were in the lower scatter band of the cast specimen due the presence of columnar grains along the testing direction. Additionally, the authors reported that the specimens extracted from the build direction approached the mean value exhibited by the cast specimens with longer test duration, whereas the specimens extracted from the scan direction tend to go astray.

7. Effects of Post-Processing

The poor weldability of high- γ' nickel-based superalloys results in the need for post processing for part densification and mitigation of defects in SLM-fabricated specimens. Hot isostatic pressing (HIP) as discussed by Kunze et al. [36] for IN738LC and by Carter et al. [18]

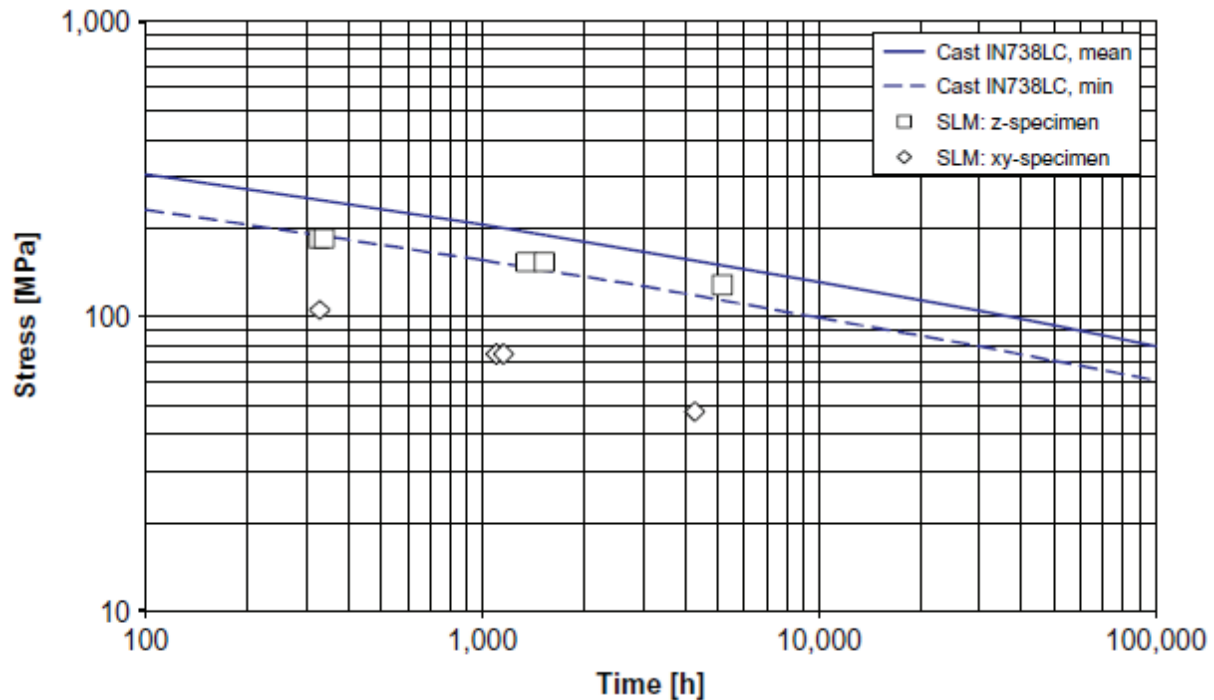


Figure 12. Comparison of stress to 1% total plastic strain data of cast and SLM processed IN738LC at 850 °C (adopted from [29]).

for CM247LC was effective in closing micro cracks. Messé et al. investigated the effects of stress relieving heat treatment (standard heat-treatment of 1120 °C for 2 h, followed by 845 °C for 16 h; both steps were followed by air-cooling) on as deposited (SLM), the stress relieved (SLM-SR), and conventionally cast (CC) IN738LC [30]. The γ' dissolution began at 1155 °C, 1160 °C, and 1150 °C, and ended at 1175 °C, 1178 °C, and 1185 °C, for the SLM, SLM-SR and CC conditions, respectively. Though all specimens shared the same solidus temperature of 1260 °C and the same liquidus temperature of 1320 °C, the differences in the γ' solvus and the range

of temperatures over which the γ' dissolution happened were due to γ' population difference as well as compositions. Messé et al. reported that the most noticeable in the SLM-SR occurred between 1040 °C and 1090 °C. A similar event was also visible in the SLM condition, through much weaker in magnitude. The absence of such endothermic flow in CC state indicated that the transition was associated with the thermo-mechanical history.

Table 6. Average sizes of the cells, grains, and precipitates of CM247LC in the as-SLM and SLM+HT (T) states. Elongated cells and grains were measured along their transverse or/and longitudinal sections, TS and LS respectively. All precipitates were measured along the TS. (adopted from [14]).

Condition	Cells TS (nm)	Cell colonies – grains		Carbides fraction (% vol)	Carbides size (nm)	γ' size (nm)
		TS (μm)	LS (μm)			
as-SLM	500	12	53	–	50	5†, 50‡
SLM+HT (1150 °C)	700	13	53	0.8	240	150†, 570‡
SLM+HT (1210 °C)	700	12	50	0.8	230	150†, 455‡
SLM+HT (1230 °C)	1100	12	48	0.8	250	860‡, 290□, 225♦
SLM+HT (1240 °C)	N/A	70	175	1.1	270	270♦
SLM+HT (1260 °C)	N/A	80	200	1.5	210	150♦

No recrystallised grains: † irregular small, ‡ irregular large, □ cuboidal. Recrystallised grains: ♦ cuboidal.

Muñoz-Moreno reported that increasing the solution treatment temperature to 1260 °C for CM247LC resulted in a reduction of the γ' precipitate size to approximately 150 nm as shown in Table 6 [14]. Hardness tests revealed that as-SLM specimens showed hardness of 409 ± 7 HV which continuously increased to 442.7 ± 16 HV for HT of 1210 °C, 437.7 ± 19 HV for HT of 1230 °C, 448.7 ± 23 HV for HT 1240 °C, and 462.7 ± 13 HV for HT 1260 °C. The authors acquired the resonant ultrasound spectroscopy (RUS) spectra from the specimens to extract the elastic stiffness coefficients, Young's moduli, shear moduli and Poisson's ratio, assuming isotropic, hexagonal, and orthorhombic average symmetries. In order to quantify the elastic anisotropy of the specimens, the hexagonal and isotropic elastic stiffness coefficients were related through three anisotropy factors A_1 , A_2 , and A_3 as

follows:

$$A_1 = \frac{2c_{44}}{c_{11} - c_{12}} \quad A_2 = \frac{c_{23}}{c_{12}} \quad A_3 = \frac{c_{33}}{c_{11}}$$

Here c_{ij} represents the elastic stiffness coefficients, assuming hexagonal symmetry. These were defined such that hexagonal symmetry reduced to isotropic symmetry when A_1 , A_2 , and A_3 were all equal 1. Figure 13 shows the elastic anisotropy factors obtained from the as-SLM and SLM+HT samples. For the as-SLM sample, and those solution treated at temperatures equal to or below 1230 °C, the three anisotropy factors obtained differed significantly from unity but were very similar to one another. These results confirmed that strong axisymmetric elastic bulk behavior existed in the as-SLM. Notably, the localized recrystallization observed in the SLM+HT (1230 °C) specimen did not result in a significant reduction in the elastic anisotropy. In contrast, the anisotropy factors of the specimens heat-treated at temperatures equal to or greater than 1240 °C were closer to unity. This indicated that the specimens subjected to the higher temperature heat treatments exhibited more isotropic behavior. Nevertheless, the deviations away

from unity in the anisotropy factors and the large RMS errors obtained when fitting the data assuming isotropic symmetry indicated that the samples heat-treated at 1240 °C and above did retain appreciable elastic anisotropy.

Rickenbacher et al. reported that at elevated temperature, specimens extracted from the scan direction showed 15% higher yield strength and 9% higher Young's modulus. The ultimate tensile strength was like cast specimens, whereas the elongation at break is 20% lower. The

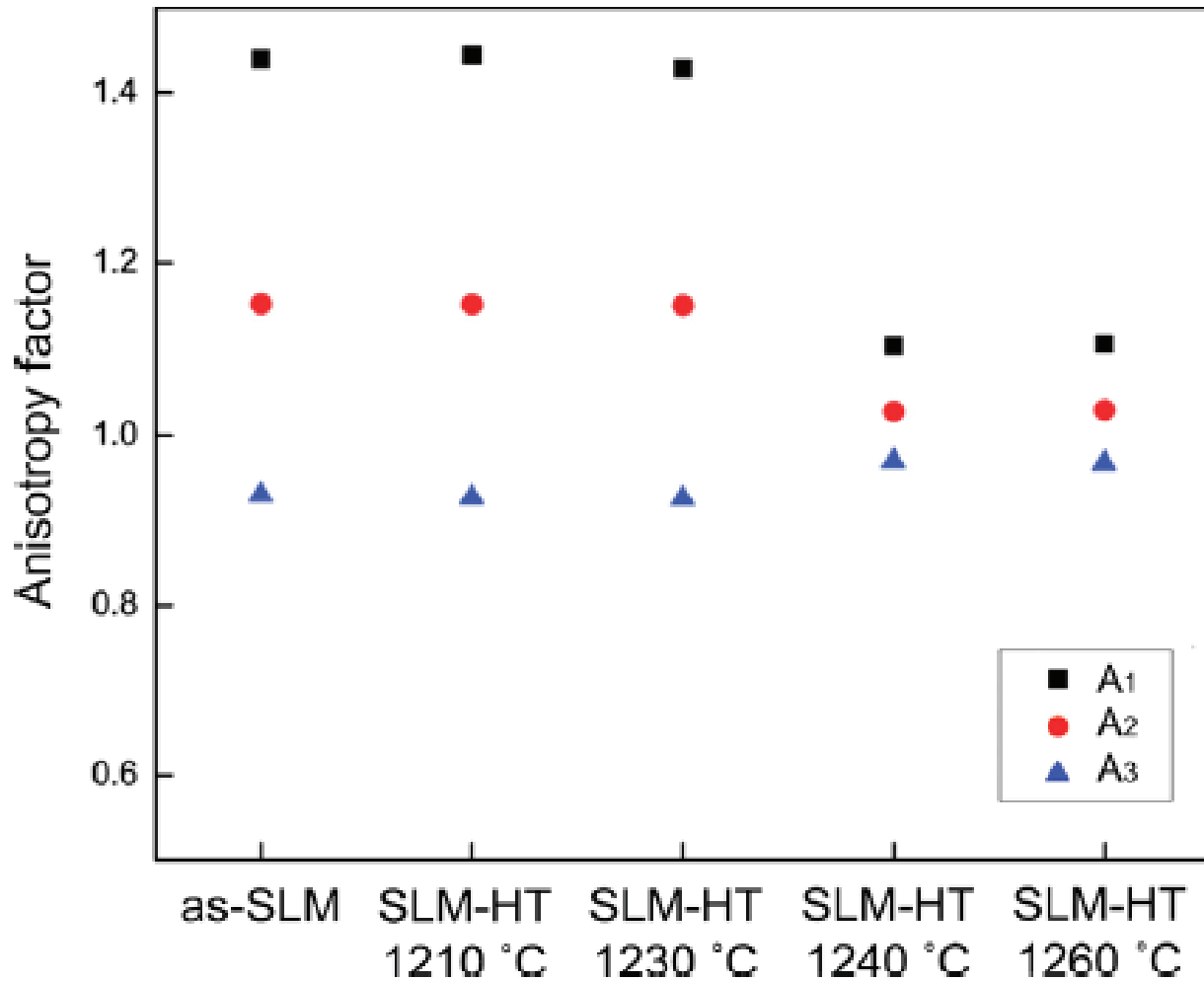


Figure 13. Elastic anisotropy factors of the as-SLM and SLM+HT CM247LC samples (adopted from [14]).

specimens extracted from the build direction showed a 24% lower Young's modulus and a 42% higher elongation in average. The yield and ultimate strength values were 5 and 3% lower compared to cast specimens, respectively.

8. Conclusions

A review of the existing literature revealed that SLM of high- γ' nickel-based superalloys has not been extensively investigated to explore and exploit the possibilities SLM offers for

fabricating high quality, low cost, repeatable, and reliable parts in automotive, aerospace, and aircraft industries. To date, the effects of the SLM process parameters and powder properties on the physical, mechanical, and microstructural behavior of high- γ' nickel-based superalloys under dynamic and coupled loading, oxidation, corrosion, and thermal conditions are yet to be fully proven. However, high- γ' nickel-based superalloys are known to be uniquely challenging because of their propensity to several types of crack formation, and therefore, tend to exhibit processing problems and metallurgical defects. The current lack of thorough understanding has been reviewed to provide a basis for further research on this important class of material system.

Consolidation regimes associated with SLM of high- γ' nickel-based superalloys have been identified for a handful of alloy system. Available literature was evaluated with a view to gaining useful insights especially in the aspect of alloying effects on the microstructure and the mechanical properties. This led to highlighting the importance of reducing oxygen content to improve part quality and property. Analysis of the available literature has led to the recognition of the influential process parameters (processing atmosphere, laser processing parameters, layer thickness, and laser energy distribution) and material properties (powder flowability and chemical composition). The process parameters and powder characteristics show strong influences on the properties of the high- γ' nickel-based superalloy parts fabricated via SLM.

9. References

- [1] T.M. Pollock, S. Tin, Nickel-based superalloys for advanced turbine engines: chemistry, microstructure and properties, *Journal of propulsion and power* 22(2) (2006) 361-374.
- [2] M. Rappaz, S. David, J. Vitek, L. Boatner, Development of microstructures in Fe–15Ni–15Cr single crystal electron beam welds, *Metallurgical and Materials Transactions A* 20(6) (1989) 1125-1138.
- [3] M. Rappaz, C.-A. Gandin, Probabilistic modelling of microstructure formation in solidification processes, *Acta metallurgica et materialia* 41(2) (1993) 345-360.
- [4] M. Henderson, D. Arrell, R. Larsson, M. Heobel, G. Marchant, Nickel based superalloy welding practices for industrial gas turbine applications, *Science and Technology of Welding Joining* 9(1) (2004) 13-21.
- [5] G. Young, T. Capobianco, M. Penik, B. Morris, J. McGee, The mechanism of ductility dip cracking in nickel-chromium alloys, *WELDING JOURNAL-NEW YORK* 87(2) (2008) 31.
- [6] A. Basak, S. Das, Additive Manufacturing of Nickel-Base Superalloy René N5 through Scanning Laser Epitaxy (SLE)– Material Processing, Microstructures, and Microhardness Properties, *Advanced Engineering Materials* 19(3) (2017) 1600690.
- [7] M. Haafkens, J. Matthey, A new approach to the weldability of nickel-base As-cast and power metallurgy superalloys, *Welding Journal* 61(11) (1982).
- [8] A. Basak, S. Das, Epitaxy and Microstructure Evolution in Metal Additive Manufacturing, *Annual Review of Materials Research* 46(0) (2016) 125-149.
- [9] T. DebRoy, H. Wei, J. Zuback, T. Mukherjee, J. Elmer, J. Milewski, A.M. Beese, A. Wilson-Heid, A. De, W. Zhang, Additive manufacturing of metallic components–process, structure and properties, *Progress in Materials Science* 92 (2018) 112-224.

- [10] Y. Kok, X.P. Tan, P. Wang, M. Nai, N.H. Loh, E. Liu, S.B. Tor, Anisotropy and heterogeneity of microstructure and mechanical properties in metal additive manufacturing: A critical review, *Materials & Design* 139 (2018) 565-586.
- [11] C. Körner, Additive manufacturing of metallic components by selective electron beam melting—a review, *International Materials Reviews* 61(5) (2016) 361-377.
- [12] C.Y. Yap, C.K. Chua, Z.L. Dong, Z.H. Liu, D.Q. Zhang, L.E. Loh, S.L. Sing, Review of selective laser melting: Materials and applications, *Applied Physics Reviews* 2(4) (2015) 041101.
- [13] V. Divya, R. Muñoz-Moreno, O. Messé, J. Barnard, S. Baker, T. Illston, H.J. Stone, Microstructure of selective laser melted CM247LC nickel-based superalloy and its evolution through heat treatment, *Materials Characterization* 114 (2016) 62-74.
- [14] R. Muñoz-Moreno, V. Divya, S. Driver, O. Messé, T. Illston, S. Baker, M. Carpenter, H. Stone, Effect of heat treatment on the microstructure, texture and elastic anisotropy of the nickel-based superalloy CM247LC processed by selective laser melting, *Materials Science and Engineering: A* 674 (2016) 529-539.
- [15] L.N. Carter, X. Wang, N. Read, R. Khan, M. Aristizabal, K. Essa, M.M. Attallah, Process optimisation of selective laser melting using energy density model for nickel based superalloys, *Materials Science and Technology* 32(7) (2016) 657-661.
- [16] J.H. Boswell, D. Clark, W. Li, M.M. Attallah, Cracking during thermal post-processing of laser powder bed fabricated CM247LC Ni-superalloy, *Materials & Design* 174 (2019) 107793.
- [17] S. Catchpole-Smith, N. Aboulkhair, L. Parry, C. Tuck, I. Ashcroft, A. Clare, Fractal scan strategies for selective laser melting of ‘unweldable’ nickel superalloys, *Additive Manufacturing* 15 (2017) 113-122.
- [18] L.N. Carter, C. Martin, P.J. Withers, M.M. Attallah, The influence of the laser scan strategy on grain structure and cracking behaviour in SLM powder-bed fabricated nickel superalloy, *Journal of Alloys and Compounds* 615 (2014) 338-347.
- [19] A. Basak, R. Acharya, S. Das, Additive Manufacturing of Single-Crystal Superalloy CMSX-4 Through Scanning Laser Epitaxy: Computational Modeling, Experimental Process Development, and Process Parameter Optimization, *Metallurgical and Materials Transactions A* 47(8) (2016) 3845-3859.
- [20] A. Basak, S. H R, S. Das, Microstructures and Microhardness Properties of CMSX-4® Additively Fabricated through Scanning Laser Epitaxy (SLE), *Journal of Materials Engineering and Performance* (2017).
- [21] R. Acharya, R. Bansal, J.J. Gambone, S. Das, A coupled thermal, fluid flow, and solidification model for the processing of single-crystal alloy CMSX-4 through scanning laser epitaxy for turbine engine hot-section component repair (part I), *Metallurgical and Materials Transactions B* 45(6) (2014) 2247-2261.
- [22] R. Acharya, R. Bansal, J.J. Gambone, S. Das, A microstructure evolution model for the processing of single-crystal alloy CMSX-4 through scanning laser epitaxy for turbine engine hot-section component repair (Part II), *Metallurgical and Materials Transactions B* 45(6) (2014) 2279-2290.
- [23] A. Basak, S. Das, Effect of Heat Treatment on the Microstructures of CMSX-4® Processed through Scanning Laser Epitaxy (SLE), *The 28th Annual International Solid Freeform Fabrication Symposium—An Additive Manufacturing Conference*, Austin, Texas, 2017.

- [24] A. Basak, S. Das, Microstructure of nickel-base superalloy MAR-M247 additively manufactured through scanning laser epitaxy (SLE), *Journal of Alloys and Compounds* 705 (2017) 806-816.
- [25] A. Basak, S. Das, Characterization of MAR-M247 Deposits Fabricated through Scanning Laser Epitaxy (SLE), *The 28th International Solid Freeform Fabrication Symposium*, Austin, Texas, 2017.
- [26] Y. Hagedorn, J. Risse, W. Meiners, N. Pirch, K. Wissenbach, R. Poprawe, Processing of nickel based superalloy MAR M-247 by means of High Temperature-Selective Laser Melting (HT-SLM), *High Value Manufacturing: Advanced Research in Virtual and Rapid Prototyping - Proceedings of the 6th International Conference on Advanced Research and Rapid Prototyping*, 2013, pp. 291-295.
- [27] R. Acharya, S. Das, Additive manufacturing of IN100 superalloy through scanning laser epitaxy for turbine engine hot-section component repair: process development, modeling, microstructural characterization, and process control, *Metallurgical and Materials Transactions A* 46(9) (2015) 3864-3875.
- [28] A. Basak, S. Das, Additive Manufacturing of Nickel-Base Superalloy IN100 Through Scanning Laser Epitaxy, *JOM* 70(1) (2018) 53-59.
- [29] L. Rickenbacher, T. Etter, S. Hövel, K. Wegener, High temperature material properties of IN738LC processed by selective laser melting (SLM) technology, *Rapid Prototyping Journal* 19(4) (2013) 282-290.
- [30] O. Messé, R. Muñoz-Moreno, T. Illston, S. Baker, H. Stone, Metastable carbides and their impact on recrystallisation in IN738LC processed by selective laser melting, *Additive Manufacturing* 22 (2018) 394-404.
- [31] M. Cloots, P.J. Uggowitzer, K. Wegener, Investigations on the microstructure and crack formation of IN738LC samples processed by selective laser melting using Gaussian and doughnut profiles, *Materials & Design* 89 (2016) 770-784.
- [32] C. Qiu, H. Chen, Q. Liu, S. Yue, H. Wang, On the solidification behaviour and cracking origin of a nickel-based superalloy during selective laser melting, *Materials Characterization* 148 (2019) 330-344.
- [33] N. Perevoshchikova, J. Rigaud, Y. Sha, M. Heilmaier, B. Finnin, E. Labelle, X. Wu, Optimisation of selective laser melting parameters for the Ni-based superalloy IN-738 LC using Doehlert's design, *Rapid Prototyping Journal* 23(5) (2017) 881-892.
- [34] R. Engeli, T. Etter, S. Hoevel, K. Wegener, Processability of different IN738LC powder batches by selective laser melting, *Journal of Materials Processing Technology* 229 (2016) 484-491.
- [35] F. Geiger, K. Kunze, T. Etter, Tailoring the texture of IN738LC processed by selective laser melting (SLM) by specific scanning strategies, *Materials Science and Engineering: A* 661 (2016) 240-246.
- [36] K. Kunze, T. Etter, J. Grässlin, V. Shklover, Texture, anisotropy in microstructure and mechanical properties of IN738LC alloy processed by selective laser melting (SLM), *Materials Science and Engineering: A* 620 (2015) 213-222.
- [37] Z. Chen, S. Chen, Z. Wei, L. Zhang, P. Wei, B. Lu, S. Zhang, Y. Xiang, Anisotropy of nickel-based superalloy K418 fabricated by selective laser melting, *Progress in Natural Science: Materials International* 28(4) (2018) 496-504.

- [38] A. Basak, S. Das, A study on the microstructural characterization of René 142 deposited atop René 125 processed through scanning laser epitaxy, *Materials Science Forum*, Trans Tech Publ, 2017, pp. 187-192.
- [39] A. Basak, R. Acharya, S. Das, Epitaxial deposition of nickel-based superalloy René 142 through scanning laser epitaxy (SLE), *Additive Manufacturing* 22 (2018) 665-671.
- [40] A. Basak, Y. Yang, S. Das, On the Spatial Variation of the Microstructure and Microhardness Properties of Nickel-Based Superalloy René 142 Fabricated via Scanning Laser Epitaxy (SLE), *Materials Performance and Characterization* 8(6) (2019).
- [41] R. Acharya, R. Bansal, J.J. Gambone, M.A. Kaplan, G.E. Fuchs, N. Rudawski, S. Das, Additive Manufacturing and Characterization of René 80 Superalloy Processed Through Scanning Laser Epitaxy for Turbine Engine Hot-Section Component Repair, *Advanced Engineering Materials* 17(7) (2015) 942-950.
- [42] A. Basak, S. Das, A study on the effects of substrate crystallographic orientation on microstructural characteristics of René N5 processed through scanning laser epitaxy, 13th International Symposium on Superalloys, SUPERALLOYS 2016, Minerals, Metals and Materials Society, 2016, pp. 1041-1049.
- [43] A. Basak, S. Das, An Investigation of Dendritic Segregation in Single-Crystal René N5 Fabricated through Scanning Laser Epitaxy, *Proc. 27th Annu. Int. Solid Freeform Fabr. Symp.*, 2016.
- [44] D. Herzog, V. Seyda, E. Wycisk, C. Emmelmann, Additive manufacturing of metals, *Acta Materialia* 117 (2016) 371-392.
- [45] I. Gibson, D.W. Rosen, B. Stucker, *Additive manufacturing technologies*, Springer 2014.
- [46] T.G. Spears, S.A. Gold, In-process sensing in selective laser melting (SLM) additive manufacturing, *Integrating Materials and Manufacturing Innovation* 5(1) (2016) 16-40.
- [47] P.K. Gokuldoss, S. Kolla, J. Eckert, Additive manufacturing processes: Selective laser melting, electron beam melting and binder jetting—Selection guidelines, *Materials* 10(6) (2017) 672.
- [48] R. Decker, J. Mihalisin, Coherency strains in gamma prime hardened nickel alloys, *ASM TRANS QUART* 62(2) (1969) 481-489.
- [49] M. Yoo, On the theory of anomalous yield behavior of Ni₃Al—Effect of elastic anisotropy, *Scripta metallurgica* 20(6) (1986) 915-920.
- [50] M.J. Donachie, S.J. Donachie, *Superalloys: a technical guide*, ASM international 2002.
- [51] S. Babu, S. David, J. Park, J. Vitek, Joining of nickel base superalloy single crystals, *Science and technology of welding and joining* 9(1) (2004) 1-12.
- [52] Z. Zhou, L. Huang, Y. Shang, Y. Li, L. Jiang, Q. Lei, Causes analysis on cracks in nickel-based single crystal superalloy fabricated by laser powder deposition additive manufacturing, *Materials & Design* 160 (2018) 1238-1249.
- [53] S. Das, Physical aspects of process control in selective laser sintering of metals, *Advanced Engineering Materials* 5(10) (2003) 701-711.
- [54] E.O. Olakanmi, R. Cochrane, K. Dalgarno, A review on selective laser sintering/melting (SLS/SLM) of aluminium alloy powders: Processing, microstructure, and properties, *Progress in Materials Science* 74 (2015) 401-477.
- [55] M. Agarwala, D. Bourell, J. Beaman, H. Marcus, J. Barlow, Direct selective laser sintering of metals, *Rapid Prototyping Journal* 1(1) (1995) 26-36.

- [56] J. Risse, C. Golebiewski, W. Meiners, K. Wissenbach, Einfluss der Prozessführung auf die Rissbildung in mittels SLM hergestellten Bauteilen aus der Nickelbasislegierung IN738LC, Proceedings of the RapidTech 2013. Presented at the RapidTech (2013).
- [57] N. Richards, M. Chaturvedi, Effect of minor elements on weldability of nickel base superalloys, International Materials Reviews 45(3) (2000) 109-129.
- [58] M. Rappaz, A. Jacot, W.J. Boettinger, Last-stage solidification of alloys: theoretical model of dendrite-arm and grain coalescence, Metallurgical and Materials Transactions A 34(3) (2003) 467-479.
- [59] H. Zhu, S. Guo, H. Guan, V. Zhu, Z. Hu, V. Murata, M. Morinaga, The effect of silicon on the microstructure and segregation of directionally solidified IN738 superalloy, Materials at high temperatures 12(4) (1994) 285-291.